Research Square

Preprints are preliminary reports that have not undergone peer review.
They should not be considered conclusive, used to inform clinical practice,
or referenced by the media as validated information.

Characterization of aerosol particles during a high pollution episode over Mexico City

Giovanni Carabali (carabali@igeofisica.unam.mx)
Instituto de Geofísica, Universidad Nacional Autónoma de México.
José Villanueva-Macías
Facultad de Química, Universidad Nacional Autónoma de México
Luis Ladino
Centro de Ciencias de la Atmósfera, Universidad Nacional Autónoma de México.
Harry Álvarez-Ospina
Facultad de Ciencias, Universidad Nacional Autónoma de México
Graciela Raga
Centro de Ciencias de la Atmósfera, Universidad Nacional Autónoma de México.
Gema Andraca-Ayala
Centro de Ciencias de la Atmósfera, Universidad Nacional Autónoma de México.
Javier Miranda
Instituto de Física, Universidad Nacional Autónoma de México
Michel Grutter
Centro de Ciencias de la Atmósfera, Universidad Nacional Autónoma de México.
Monserrat Silva
Centro de Ciencias de la Atmósfera, Universidad Nacional Autónoma de México.
David Riveros-Rosas
Instituto de Geofísica, Universidad Nacional Autónoma de México.

Research Article

Keywords: atmospheric pollution, aerosol particles, environmental science

Posted Date: June 4th, 2021

DOI: https://doi.org/10.21203/rs.3.rs-570917/v1

License: This work is licensed under a Creative Commons Attribution 4.0 International License.
Read Full License

Version of Record: A version of this preprint was published at Scientific Reports on November 18th, 2021. See the published version at https://doi.org/10.1038/s41598-021-01873-4.

Abstract

More than 7 thousand wildfires were recorded over Mexico in 2019, affecting almost 640 thousand hectares. Most of these fires occurred during the warm-dry season generating dense smoke plumes, impacting urban areas in the central part of the Mexican plateau. From May 10 to 17, 2019, biomass burning (BB) plumes affected Mexico City (MC) and diffused across the basin, drastically reducing visibility. Due to the severity of this high atmospheric pollution (HAP) episode, the local government declared an environmental contingency, warning the population. Fine particle ($PM_{2.5}$) concentrations were ~ 2 times higher than the nation's air quality standards. Likewise, aerosol optical measurements indicated that visibility was mainly affected by fine aerosol particles. Electron microscopy analysis of aerosol samples obtained during the HAP days shows a high incidence of strong absorbent soot and tarballs (TB). These types of particles were simultaneously observed in MC and at the high-altitude Altzomoni Atmospheric Observatory (~ 4010 m.a.g.l.). Elemental analysis of the particles shows that the composition is dominated by sulfur and potassium, evidencing a strong influence of the BB emissions, but also suggests the presence of urban pollution from MC at the remote Altzomoni site.

Introduction

Atmospheric aerosols can affect the planet's radiation balance by scattering solar radiation, which results in the cooling of the Earth's surface [1,2]. These particles can also indirectly affect climate, based on how they interact with surrounding clouds [3–5]. The direct effects of aerosols on the climate system are much better understood and quantified than the indirect effects. Furthermore, aerosol particles are of interest due to their effects on human health and regional visibility [6,7].

High atmospheric pollution (HAP) episodes were very frequent in Mexico City (MC) in the 90s [8,9]; however, the systematic measures implemented to mitigate urban emissions over the decades have significantly decreased their occurrence. MC was affected by a severe pollution episode in May 2019, which was detected by several stations of the Automatic Atmospheric Monitoring Network (RAMA by its acronym in Spanish). The concentrations of $PM_{2.5}$ presented a rapid and dramatic increase from May 10 to 17. The 2019 HAP episode significantly reduced the visibility (V_a) and degraded the air quality in MC, a fact that alarmed MC's authorities, who decreeing an environmental contingency to mitigate their impacts. The MC metropolitan area (MCMA) formed by MC, adjacent municipalities, and other urban zones from the State of Mexico and Hidalgo, is considered one of the largest emission sources of atmospheric pollutants in the central Mexico plateau[10,11]. Additionally, the MCMA may be affected by the regional transport of pollutants mainly during the dry-warm season (February to May), when a large number of wildfires occur in Mexico and Central America [12–14].

In order to understand the role that aerosol particles play in the climate system, it is important to monitor and characterize their physicochemical and optical properties. A quick assessment of the air quality in a given region can be done by measuring V_a, which indicates the visual range that can be perceived by the

human eye [15]. This parameter is calculated from the extinction coefficient (β_{ex}) using the Koschmieder equation[15], but it is also estimated from aerosol optical depth (AOD) measurements [15]. The AOD parameter measured by the Aerosol Robotic Network (AERONET) represents the vertically integrated extinction coefficient in the atmospheric column. Simultaneous analyzes of the aerosol morphological properties and their elemental composition is an alternative to characterize them [2,16–19]. While particle shape can be associated with their size and optical properties, the elemental composition is related to their origin and mixing state. Based on their composition and morphology, urban aerosol particles can be classified as soot, tarballs (TB), mineral dust, S-rich and K-rich, sea salt, metallic, among others [20–22]. This classification can be performed by using Transmission- (TEM) and Scanning electron microscopy (SEM) techniques coupled with the energy dispersed X-ray detector (EDX or EDS) [19,20,23].

This study characterizes particles sampled simultaneously in MC and at the high-altitude Altzomoni atmospheric observatory (AAO) during the HAP event from May 10 to 17, 2019. The main objective of the study was to identify the primary sources of aerosol particles that significantly reduced air quality in MC by performing an optical, morphological, and chemical characterization.

Results And Discussions

Heavy aerosol pollution episode in Mexico City

The central part of Mexico during the dry-warm season is dominated by an anticyclonic system, which leads to sunny, warm weather and low precipitation in the MCMA [24,25]. These hot and dry conditions favor the presence of dust and BB emissions from wildfires [12]. Nearly 7,410 fires and almost 589,371 hectares burned were reported in Mexico during 2019 (CONAFOR, 2020) [26]. Figure 1 shows the location of active fires in Mexico detected by the Visible Infrared Imaging Radiometer Suite (VIIRS) on May 11, 12, 14, and 15. Fires occur throughout Mexico but are concentrated in the western, central, and southwestern regions. Satellite imagery shows the dense smoke plumes emitted by the wildfires, which reached the central Mexico plateau. There were also a significant number of fires that occurred inside and around the Mexico City basin.

Figure 2 shows the 24-hour average $PM_{2.5}$ concentration measured during May 2019 in four RAMA stations: CCA, GAM, MER, and TLA in MC. All stations located in different parts of the MC (see Fig. 11c), registered a drastic increase in 24-hour average $PM_{2.5}$ from May 10 to 17. The 24-hour $PM_{2.5}$ mean concentration at the CCA station during HAP days was 65.1 μgm^{-3}, which significantly exceeded the Mexican national air quality standards of 45.0 μgm^{-3}. That $PM_{2.5}$ increment during the HAP episode began on May 10 reaching the maximum concentrations on May 12 and 13 with peak $PM_{2.5}$ values of 81.9 and 86.8 μgm^{-3}, respectively. The decrease in the concentration of these particles was observed from May 17, with average values < 40 μgm^{-3}.

Aerosol optical depth and visibility

Figure 3 (a) shows the average AOD over daytime measurements at 6 different wavelengths (340, 380, 440, 500, 675, and 870 nm) during May 2019, with the highest AOD values observed from May 14 to 18. Due to technical failures, the sensor did not report data the second week of May, including the beginning of the HAP episode. Nevertheless, for the remaining days of the HAP episode (from 14 to 18) high AOD values were observed, with maxima of 0.90, 0.91, and 0.78 measured on May 15, 16, and 17, respectively. These maximum values are ~ 3 times higher than the annual mean AOD (0.32) registered during May 2019. These AOD peaks are caused by the high aerosol loading, evidenced by the $PM_{2.5}$ measurements (Fig. 2). Although all aerosols contribute to the AOD increase, the SDA calculations suggest that the AOD variability in MC is dominated by FM particles. Fig. 3 (b) shows the trend of the FM and CM contribution to the AOD (500 nm) measured during May 2019. The FM AOD during the entire month ranges between ~ 0.20 and ~ 0.95, while CM AOD varies between 0.01 and 0.03. Carabali et al. (2017)[10] reported similar SDA results in MC, demonstrating that fine particles highly contribute to AOD. Similarly, another study of aerosols in the MC during spring 2019 found that fine particles originate mainly from BB and local traffic emissions, while the primary source of coarse particles is dust from re-suspended soil dust [27].

A remarkable reduction in V_a was also noted in MC during the HAP event. Figure 4 shows the scatter plot of AOD at 500 nm and both V_a calculations (i.e., β_{ext} and AOD_{500}), where a good correlation for Z_i = 3.0 km was obtained. The impact of the atmospheric pollution on V_a can be estimated for the 7 days of the HAP period, as seen in Table 1 for 24-hr averages, V_a suffered a degradation greater than 80% during the HAP days, highlighting the high absorption of particles that affected MC in May 2019.

Table 1. Average values of $PM_{2.5}$ concentration (CCA measurements), AOD, and V_a during HAP days (from 10 to 17 May 2019), low-pollution days (01 – 09 and 18 – 31 of May 2019), and annual means.

	$PM_{2.5}$ (μgm^{-3})	AOD	V_A from β_{ext} (km)	V_A from AOD (km) Z_i = 1.0, 1.5, and 3.0
Highly polluted days	65.1 ± 13.6	0.80 ± 0.13	10.3±3.8	4.9±0.1, 7.3±1.2, and 14.7±2.4
Low pollution days	29.4 ± 7.2	0.43 ± 0.16	60.5±15.1	9.1±3.4, 13.4±5.1, and 27.3±10.1
Annual mean	20.9 ± 13.6	0.30 ± 0.12	-----	----

Individual TEM analysis of the aerosol particles sampled in MC during the HAP episode confirms its strong absorbent feature (Fig. 5). TEM micrographs show particles with different sizes and morphologies. For example, Figure 5a shows spherical particles with diameters (d_p) <1 μm. These particles have an elemental composition dominated by a strong C signal and minor O (Fig. 5c), a characteristic composition of tarballs (TB), a type of particles that originate from the incomplete combustion of fossil fuels or biomass [16,28]. Although it is difficult to know the origin of these TB particles, due to the various

sources within MC, BB emissions may be the largest TB contributor. Fig. 5b shows the TEM image of a soot aggregate with a morphology very different from that exhibited by TB particles. The soot particles are composed of nanometric carbon spherules that join together to form chains and clusters with d_p > 1 μm; its EDS spectra consist mainly of C, O, and high-intensity signals of K and S (Fig. 5d).

Aerosol effect on global solar irradiance

The influence of aerosols on daily solar irradiation is analyzed in Figure 6. The observed increase in $PM_{2.5}$ concentrations from 10 to 17 May had an obvious effect on GHI (Fig. 6a, shaded period). The data indicate that GHI gradually decreases as $PM_{2.5}$ levels increased, mainly due to the scattering and absorption of sunlight[29]. The significant reduction in irradiance occurs mainly between 11:00 h and 18:00 h LST (Fig. S1a), when maximum irradiance values are detected, coincides with the highest presence of smoke. To quantitatively estimate the $PM_{2.5}$ impact on the solar irradiance, the maximum daily GHI measurements were subtracted from the monthly mean GHI_m value. This difference ($\Delta GHI = GHI - GHI_m$) taken as an anomaly in percent (or departures from the mean monthly value) has a direct impact on visibility. Figure 6b shows the ΔGHI and the $PM_{2.5}$ trends, where it can be observed that the maximum GHI has a significant reduction due to the increase of the $PM_{2.5}$ levels. This high load of aerosol particles during the HAP days resulted in a significant loss of 17 % in the GHI. The monthly mean value of the GHI measured experimentally (1130 ± 66 Wh/m²) fits well with the value calculated theoretically with the ESRA clear sky model [30] (i.e., 1108 Wh/m²) that represents the typical GHI value for this month in MC, according to the Linke turbidity value (equal to 4) reported for SODA web services (http://www.soda-pro.com/). Figure S1b shows the correlation between these quantities, with a correlation coefficient of 0.54. The negative tilt matches solar irradiation reduction, corresponding with the $PM_{2.5}$ values increasing. The average values of the GHI and its anomaly during the HAP period and during the low polluted days of May 2019 are shown in Table S1.

Aerosol characterization at AAO

Vertical transport of pollutants within the mixing layer

Ceilometer measurements were used to estimate the height of the ML, required to infer the vertical distribution of aerosols. The derivation of the ML height during spring is reliable due to suitable meteorological conditions (low humidity, clear skies, and the absence of precipitation) and high aerosol loading in the atmosphere. Figure S2 shows the resulting profile of the ML height estimates for the MC on May 14, 2019. The sharp decrease in aerosol backscattering between the ML and FT (contrasting colors in Fig. S2a) indicates the boundary between the ML and the free troposphere. The ML time series starts in the early morning hours, with an average height of 900 m a.g.l, until midday when it increases rapidly, reaching heights > 3500 m a.g.l. due to turbulence and dry convective processes. The ML collapses after sunset, as seen in the height decrease around 18:00 LST. ML expansion was also evident with the increase in particle concentration at the AAO. Figure S2b shows the total particle concentration (sizes > 30 nm) measured with a condensation particle counter (CPC) at the AAO. A rapid increase in particle

concentration was observed at 11:00 LST, and subsequently, the maximum value was reached at 11:30 LST. Similar results were published by Baumgardner et al. (2009) [22], who found that particulate matter concentration and other pollutants reach their maximum concentration at mid-afternoon.

Aerosol particle types at AAO

Analysis was carried out on 120 particles and based on the morphology and elemental composition as the main criteria, allowing the particle classification into five groups (Table 2): soot, organic, mineral dust, S-rich, and complex secondary particles. Statistical analysis of the spectra showed that 90% of the particles contain C and O, 50% of the particles contain Si, and 30% present S. Fe and Al were also detected although in a low number of particles with weak signals. Both elements (Fe and Al) were observed encapsulated by carbonaceous material, silicate coatings, or mixed with other minerals such as Ca and Na. Copper was not considered for this classification because this element is present in the TEM grids. Particle shape was considered the main factor for discriminating between soot (chain aggregates) and TB (spherical particles) particles, which were present in almost all analyzed TEM-grids.

Soot

Figure 7 shows TEM images of individual soot particles sampled at the AAO site within the FT (i.e., 12:00 – 05:00 h) during the HAP days. All images show chain-like agglomerated structures of nano-sized primary spherical particles with d_p < 60 nm, a typical structure present in soot originated in combustion processes [18]. Those soot particles sampled at the AAO could probably have been produced by BB events or were transported by the ML convective process. The soot particle in Fig. 7a has a d_p of ~ 1.6 µm, while the particle in Fig. 7b with a d_p ~ 0.7 µm is attached to the bigger one and more compact aerosol. EDS spectra in Fig. 7b consist mainly of three peaks; the most intense is the amorphous carbon signal (~ 0.28 Kev), Si and oxygen (~ 0.53 Kev). However, other peaks observed in the EDS (i.e., S and Cl) show the mixed state of the soot. Figure S3 shows an SEM image and the EDS elemental composition mapping of soot particles sampled in the AAO within the ML. The EDS map shows the presence of Si, Al, K, Ca, and Fe, homogeneously distributed throughout the particle which indicates that this particle is an aged aerosol. The high percentage of Si, Al, and O suggests the presence of material with a geological origin that resulted from the resuspension of soil dust.

Table 2. Aerosol groups observed in the AAO

Particle group	Particle type	Elemental Composition	Particle morphology
Soot	Soot or black carbon (BC)	Strong C signal in EDS spectra. Minor O and S	Particle aggregate, chains formed by nanometric carbon spherules.
Mineral dust	Mineral	EDS spectra are dominated by the Si signal. Particles containing Al and Fe. Minor signals of K, S, C, and O are observed.	Compact and irregular particles.
S-rich	Mainly soot and particles with Si	Dominated by C, have an intense S signal. The signal of Si and O were common in this group.	Particles have very irregular shapes. These aerosols are sensitive to a strong electron beam.
Organic	TB	Mostly tarball particles. Intense C signal followed by a low signal of O.	Spherical particles.
Secondary		In this group, all particles present an S signal. They contained C, O, S, and minor K.	Irregular shape particles, susceptible to beam damage. Some Ca-S particles mix with mineral, and some mix with S-rich and K-rich particles.

Mineral dust particles

Mineral dust aerosol at the AAO comes mainly from the resuspension of soils and probably from rocks eroded by the wind. These particles with d_p < 600 nm (Fig. 7 c y d) show compact shapes and are mixed with other inorganic materials. Figure 7d shows the elemental composition of a mineral particle where a high Si signal is observed, which dominates the composition of mineral particles in this region. Additionally, the mineral particles were found to be mixed with small amounts of aluminosilicates, iron-rich dust, K, and minor Ca. These elements could show the presence of feldspars whose main source could be the erosion of the rocks or could be the result of volcanic emissions [31]. The volcanic ash emitted by the Popocatepetl is one of the main components of the soils that surround the AAO. Although during the sampling days there was no direct influence of the volcanic plumes, the soils surrounding the AAO are covered with material emitted previously. The elemental EDS map in Figure S4 for a dust particle shows a homogeneous distribution of Si, Al, Mg, and Fe which demonstrates the geological origin of that particle. The presence of C and K with a uniform distribution also indicates that this particle is covered with organic material possibly originated from BB.

S-rich particles

Sulfur is one of the most frequently observed elements in the EDS spectra of particles measured at the AAO. The S present in the particles mainly comes from three sources: gas emissions from the Popocatepetl volcano, anthropogenic emissions from MC, and BB emissions. Volcanic emissions are the most important due to the proximity of the AAO to the volcano, which is known as one of the largest sulfur dioxide (SO_2) sources in the world [32,33]. Volcanic plumes consist of gases and sub-millimeter particles[32,33]. Figures 7e and 7f show TEM images of S-rich particles sampled at the AAO during HAP days. S-rich particles present different morphologies with d_p < 800 nm. All S-rich particles observed in this study suffered decomposition or evaporation as the microscope beam hit the particles, indicating that these particles are beam-sensitive and undergo some changes in their shape during analysis.

TB

Figure 8 shows TEM images (Fig. 8a) and the EDS spectrum (Fig. 8b) of the spherical organic particles with d_p < 600 nm, which was common in all aerosol samples collected at the AAO site. Those TB are particles with a special morphology (near-spherical) and composition (amorphous carbonaceous material) which are quite abundant in biomass smoke plumes [16,34,35]. These particles in the Altzomoni mountain could have two origins: anthropogenic emissions in nearby urban areas and emissions due to BB. EDS spectra in Fig. 8b confirmed the occurrence of TB at the AAO during the HAP episode. We believe that the main source of TB at the AAO is the wildfires near the sampling area. However, in previous studies, a possible large-scale transport of BB particles was evidenced [12,13].

Complex secondary particles

A significant number of secondary aerosol particles were also measured at the AAO. These particles are characterized by having complex elemental compositions and very irregular shapes (with d_p between 0.5 µm and 1.6 µm). Two types of secondary particles predominated in the analysis: particles rich in K and S. Figures 8c and 8d show two examples of secondary particles, where one of them presented S and K (Fig. 8d). The main sources of these particles can be anthropogenic emissions in urban areas and BB emissions. Particles were observed to be easily damaged by the strong electron beam, which evidences the decomposition of volatile compounds. Figure 8d shows the EDS spectrum of a secondary particle in where S has a significantly high signal with an intense peak of K. Most of the particles analyzed in this study are internally mixed, which evidences the presence of aged particles. However, it also was observed aerosol assemblies externally mixed, during the FT hours. Fig. S5 shows an example of an externally mixed particle with a soot aggregate surrounded by other particles with different compositions (mainly S). The inset in Fig. S5 is a high magnification image of an internally mixed soot coated with S and K.

Elemental composition

A comparison of the elemental composition of $PM_{2.5}$ particles sampled at the AAO and MC is shown as pie charts in Figure 9. The main elements detected with the XRF analysis were Al, Si, P, S, K, Ca, Mn, Fe, Ni, Cu, and Zn. Figure 9a shows the elemental analysis of the particles sampled at the AAO, where the

composition is dominated by S and K with percent of 46% and 35%, respectively. The abundance of these elements suggested an important contribution of the emissions from wildfires, mainly the K, which is a tracer of BB [36,37]. The existence of dust-like aerosol could be evidence by the presence of Si and Fe with significant contributions of 5% and 10%, respectively, in addition to minor contributions of Al, Mn, and Ca. Although the AAO is located in a remote rural area, small amounts (<1%) of Ni, Cu, and Zn were measured. These elements could be related to anthropogenic sources close to the sampling site (e.g., chimney of the TV-broadcast antenna facility). Figure 9b shows the elemental composition of particles sampled in MC, which presents values very similar to those measured in AAO, i.e., with S and K as the elements contributing more to elemental composition with percentages of 37% and 38%, respectively. Although S can be the product of BB, it can also come from other anthropogenic sources (i.e., motor vehicles), being the main element responsible for the production of secondary aerosol particles [37,38]. Mineral-dust aerosol is generally a significant component during the dry-warm period [39,40]. The presence of Fe and Si with percentages of 10 % and 7 %, respectively, is the primary evidence of mineral dust particles. That mineral fraction in MC is partially a result of the MC semi-arid areas (e.g., former Texcoco and Chalco lakes), arid hills, and unpaved roads within the MC basin [27,41]. The significant Ca contribution could be due to fly ash emissions from two sources: construction activities and soil-dust resuspension [27]. Furthermore, the trace elements with percentages less than 1% (Ni, Cu, and Zn), have been associated with the emissions generated by high traffic in the urban area. For example, most of the Zn detected could originate from the wear of vehicle tires, while Ni and is a typical element in motor fuel additives [27]. The elemental compositions of the particles at both sites (AAO and MC) do not show significant differences. This similarity in the percentage composition could result from the influence of aerosols emitted in the MCMA, which are transported to the AAO by advective processes in the ML[42] and orographic forcing. Note that the sampled $PM_{2.5}$ for this analysis was collected every 24 hours, making it impossible to separate the TL and BL periods. Excluding the organic materials (not measured in this study), the elemental composition of the aerosol at both sites was dominated by S and K, contributing > 75%, which evidence the strong influence of BB emissions. The present results are consistent with those reported by Decarlo et al. (2008) [11], who observed elevated sulfate at the higher altitudes above MC. Similar studies of aerosol chemical composition conducted at other high-altitude sites in different parts of the world (in the absence of BB emissions) reveal that aerosols in the FT contain a high fraction of sulfates [11,43,44].

Air masses back-trajectories

BB smoke is one of the main atmospheric components affecting air quality and climate in Mexico due to massive plumes that can travel thousands of kilometers downwind [12,13]. Tracking of these plumes is only possible through satellite measurements, e,g, by the VIIRS radiometer [45]. The HYSPLIT model was used to identify the origin of the air masses reaching the sampling sites. Figure 10 shows the HYSPLIT back-trajectories computed at different heights (100, 500, and 1000 m a.g.l.) during the HAP days (May 14 – 17 2019). The HYSPLIT simulations show that during the HAP episode the air masses mainly originate in western and southwestern Mexico where most of the active fires are concentrated (see fire distribution in

Fig. 1) to reach the AAO. However, these air masses also cross over Morelos State, where the cities of Cuautla and Cuernavaca are located, possibly indicating not only volcanic but also urban emissions in the air mass reaching the AAO. Only on May 17 there was a possible transport from north of the AAO, carrying particles emitted in CM.

Conclusions

The impact of the severe air pollution episode that affected MC for 7 days (from October 10 to 17) was evidenced from a variety of sources. $PM_{2.5}$ concentrations in four RAMA stations showed that the HAP event affected the entire urban area of MC. The 24-hour average of the $PM_{2.5}$ concentrations during HAP was 65.1 μgm^{-3}, a value ~ 1.5 times higher than the Mexican environmental standard (45 μgm^{-3}). However, maximum values of 81.9 and 86.8 μgm^{-3} registered in the CCA station on May 12 and 13 demonstrate the severity of this atmospheric pollution event. AOD (at 500 nm) measurements as part of AERONET corroborated the high aerosol loading during these polluted days with maximum values of 0.90, which is ~ 3 times greater than the annual mean AOD (0.32). The SDA results suggest that the extinction of solar radiation was mainly dominated by fine-mode particles. It was observed that the horizontal visibility (V_a) derived from extinction coefficient (β_{ext}) values suffered a significant reduction from 60.5 ± 15.1 in low aerosol concentration to 10.3 ± 3.8 km during the HAP days, while the vertical V_a estimate from AOD (Zi = 3.0 km) decreased from 27.3 to 17.7 km. The drastic reduction observed in visibility is mainly caused by the presence of absorbing fine particles as revealed by the SDA results. Likewise, the high concentration of aerosols generated a significant reduction in the GHI, which resulted in a 17% loss of irradiation.

TEM analysis on aerosol particles revealed five particle types: soot, organic, mineral dust, S-rich, and complex secondary particles. Soot was predominant in all samples analyzed, with varying degrees of mixing. EDS spectra revealed that most of the soot was mixed with relatively high amounts of S, K, and Si, likely indicating aged particles. In addition, the presence of spherical organic TB particles was evident in all TEM grids. It is not easy to establish the source of the TBs, as they were detected in both AAO and MC sites. However, we believe that the primary sources of these particles are the wildfires that affected the region in May 2019. No significant differences in the XRF elemental composition, dominated by the presence of S and K, were observed between MC and the AAO. This result is another evidence of the BB impact on aerosol chemistry at the regional level. Vertical transport of aerosols in the ML can also explain these similarities in elemental composition, which was evidenced by a substantial increase in the number of particles in the AAO during the diurnal growth of the ML. The presence of Si and Fe in significant amounts at both sites demonstrates the presence of mineral dust. In MC these dust particles come from arid soils and agricultural areas, while at the AAO, it is mainly due to soil associated with ancient volcanic ash deposits. Other anthropogenic sources that made minor contributions to the elemental composition of particulates at both sites during the HAP episode were construction activities (that release Ca) and vehicle engines (that emit Ni, Cu, and Zn).

Finally, this study successfully combined remote sensing and laboratory aerosol analysis techniques to demonstrate that the environmental contingency that occurred in MC during the spring of 2019 was mainly due to high loads of absorbing particles emitted primarily by wildfires. Despite the tremendous progress in air pollution management in MC, air pollution continues to affect the daily lives of its inhabitants and endanger their health. More effective strategies should be planned to reduce wildfires, to prevent similar episodes in the future.

Methods And Instrumentation

A direct comparison of the locally emitted particles vs. the long-range transported aerosol particles into the MCMA was assessed at the high-altitude AAO [42,46,47]. Given that the AAO is ~ 4010 m a.g.l. (and 1500 m above MC) [42,48], it allows the collection of aerosol particles within the free troposphere (FT) and the mixed layer (ML) [42,49]. Due to its location and its research facilities, the AAO is part of the Network for the Detection of Atmospheric Composition Change (NDAC) since 2015 [42,49,50]. Studies conducted at AAO have focused on volcanic emissions [32,33,51], ML pollutants [42,46], and mixed-phase cloud formation [48].

Sampling site

Altzomoni Atmospheric Observatory

The sampling was carried out at the AAO (19.117°N, 98.654° W), located approximately 60 km southeast of MC, 70 km northeast of Cuernavaca, and 50 km west of Puebla (Fig. 11). Its proximity to the active Popocatepetl volcano (~ 12 km), makes the AAO a strategic site for studying the impact of volcanic activity on the atmosphere. Altzomoni mountain is generally above the ML from late evening until late morning [42,46,47]. Ceilometer and radiosonde measurements show that the height of the ML increases rapidly between 11:00 and 13:30 local standard time (LST), with an average growth rate of more than 600 m per hour. After 13:30 LST the growth rate abruptly slows down. Garcia-Franco et al. (2018) [23] and Whiteman et al. (2000)[24] concluded that the maximum height reached by the ML is > 3 km a.g.l during the dry-warm season (March-May).

Near pristine conditions are observed at the AAO during the rainy season, whereas biomass burning (BB) prevails during the dry season [12,13,52,53]. At the altitude of the AAO surrounding areas are dominated by tall grasses. Due to the ML diurnal growth, the AAO site is affected by anthropogenic emissions generated in the MCMA[39,42]. Additionally, is may also be affected by ash and volcanic gases generated by Popocatepetl degassing and explosions [33,42,51,54]. Remote sensing studies of the volcanic plumes have revealed that SiF_4, SO_2, HCl, HF, H_2S, CO, CO_2, and H_2O are commonly emitted [33,51,55].

Aerosol Sampling system

Aerosol particles were collected directly on TEM grids (200-mesh, Gilder Cu-grids from Ted Pella Inc. USA). The TEM grids were placed on hydrophobic glass coverslips (HR3- 215; Hampton Research) by

fixing them with double-sided adhesive carbon tape. Subsequently, the glass coverslips were placed in stages 5 and 6 (cut sizes of 1.0 and 0.56 µm, respectively) of an 8-stage Micro Orifice Uniform Deposit Impactor (MOUDI, Model 100R, MSP Corp.) [56]. The glass plates were fixed onto the MOUDI stages by substrate holders, as reported by Córdoba et al. (2021)[57]. The MOUDI inlet flow was calibrated before sampling to 30 L/min using a Gilibrator air flow calibrator (Sensidyne, Inc., Clearwater, Florida, USA). A four-hour sampling period was selected to avoid particle agglomeration on TEM grids and to allow better analysis of individual particles. After each sampling, the glass coverslips with the TEM grids were stoked in sterilized Petri dishes at 4°C. Additionally, $PM_{2.5}$ samples were collected onto Teflon filters with a MiniVol sampler (AirMetrics) over 24 h periods at a flow rate of 5 L min^{-1}.

Fine Particulate Matter ($PM_{2.5}$) Measurements

Continuous $PM_{2.5}$ concentrations were obtained from the RAMA (http://www.aire.cdmx.gob.mx) using the beta-attenuation methodology. The RAMA air quality network has 30 stations deployed throughout MC. Additionally, the RAMA has a laboratory for equipment maintenance and calibration. $PM_{2.5}$ concentrations for this study were obtained from the following 4 monitoring stations (Fig. 11c):

- Centro de Ciencias de la Atmósfera (CCA) station, located in the south of MC.
- Gustavo Madero (GAM) station, located in the northern-central part of MC (downtown).
- La Merced (MER) station is located in the central-eastern region of MC.
- Tlalnepantla (TLA) is in the north of MC.

Aerosol morphology and elemental analysis

TEM, SEM, and EDS analysis

The electron microscopy analyses were performed at the Central Microscopy Laboratory of the Institute of Physics of the UNAM (IFUNAM). Electron microscope images for morphological characterization were taken in a high-resolution TEM, JEOL JEM-2010F microscope (FasTEM, JEOL, Tokyo, Japan) operated at 200 kV near the Scherrer focus, with a theoretical point-to-point resolution of 0.20 nm and a spherical aberration of 0.5 mm. TEM images were recorded with a charge-coupled device (CCD) camera and processed with the GATAN digital micrography system (version 3.7.0, Roper Technologies, Inc., Sarasota, FL, USA). SEM images were obtained with a field emission ultra-high-resolution SEM JEOL-JSM-7800F equipped with an Oxford Instruments Energy-dispersive X-ray Spectroscopy (EDS, Oxford Instruments, Abingdon, Oxfordshire, UK) detector and the AZtec 2.1 analysis software. The SEM operating voltages depend on the substrate and fluctuated between 1 and 10 kV. Micrographs obtained with SEM and TEM were analyzed using the ImageJ and Scion 4.0 software, which are public domain.

X-Ray Fluorescence (XRF) analysis

A custom-built XRF spectrometer for environmental applications equipped with an X-ray tube with Rh anode operated at 50 keV and 500 μA (Oxford Instruments, Mountain View, CA, USA) was used for $PM_{2.5}$ elemental analysis. The detection system consisted of an Amptek X-123SDD spectrometer with a resolution of 120 eV at 5.9 keV. The Teflon filters (Whatman) with $PM_{2.5}$ samples collected with a MiniVol (AirMetrics) from 12 h at a flow rate of 5 L min^{-1} were placed in the analysis chamber at a high vacuum (10−6 torr). The XRF spectrum was collected for 900 s and subsequently integrated with the Quantitative X-ray Analysis System (QXAS). The XRF spectrometer calibration procedure was achieved using thin-film standards (MicroMatter Co., Vancouver, Canada), irradiated for 300 s under the same conditions as the sample analysis. Then, accuracy checks were performed using the NIST standard reference material 2783[27,58].

Extinction coefficient and AOD measurements

Measurements of the β_{ex} were obtained from the database of the University Network of Atmospheric Observatories (RUOA, for its acronym in Spanish) https://www.ruoa.unam.mx.[49]. The β_{ex} is obtained from a Photoacoustic Extinctiometer (PAX) (Droplet Measurement Technologies, Boulder, CO), operated at a flow rate of ∼1 L min^{-1}, which is a sensitive and high-resolution instrument that measures the optical properties of aerosol particles[59]. The PAX uses a 532 nm diode laser to simultaneously measure absorption and scattering coefficients.

AOD measurements were performed with a CIMEL sun-photometer (CE-318) associated with AERONET [60] and located at the UNAM main campus in southern MC. The CE-318 device is a spectral radiometer (340, 380, 440, 500, 675, 870, and 1020 nm) programmed to automatically track the Sun following scheduled procedures to estimate the AOD. All measured optical parameters can be download from the AERONET database (https://aeronet.gsfc.nasa.gov), as well as the fine- (FM) and coarse-modes (CM) contributions to the total AOD, estimated via the Spectral De-convolution Algorithm (SDA) [61,62]. Cloud-screened (Level 1.5) data, following the methodology described by Smirnov et al. (2000) [63], was used in this study.

Estimation of the visibility

V_a is defined as the maximum horizontal distance that the human eye can see. In the present study V_a was calculated from β_{ex} values by using the Koschmieder equation (Eq. 1) [15]:

$$V_a = 3.912\,\beta_{ext}^{-1}, \qquad (1)$$

where β_{ex} is the extinction coefficient measured at 532 nm.

Additionally, V_a was calculated using Equation 2 from Baumer et al. (2008)[15], assuming β_{ex} independent of height (i.e., along the atmospheric vertical column). This estimate also assumes that all aerosol is located within the mixing layer with a height Z_i.

$$V_a = 3.912\,(Z_i)\,AOD_{500}^{-1}, \qquad (2)$$

where the mixing layer height (Z_i) was considered constant with values of 1.0, 1.5, and 3 km taken from Ceilometer measurements (See 2.8). AOD_{500} is the AOD at 500 nm measured by the CIMEL sun-photometer.

Global Solar Radiation measurements

Hourly Global Horizontal Irradiation (GHI) was calculated with the global solar irradiance measurements (I_{gg}) from the Observatory of Solar Radiation (OSR) on the Institute of Geophysics at the National Autonomous University of Mexico in Mexico City. The CMP22 radiometer (Kipp & Zonen) samples every 4 seconds and reports the average every minute. Equation 3 shows the calculation of the solar irradiation.

$$GHI = \int_{t1}^{t2} I_{gg}\,dt \qquad (3)$$

To determine the influence of atmospheric suspended particles on reduced solar irradiance, the GHI maximum values for every day were correlated with the corresponding $PM_{2.5}$ values. The average daily maximum GHI registered for May was calculated and subtracted from the maximum irradiation values of each day. This allows observing the solar radiation reduction during the HAP days.

Additionally, solar irradiances under cloud-free sky conditions for the CCA station in MC were calculated with the European Solar Radiation Atlas (ESRA), which is used in the Heliosat-2 model [30]. ESRA is an empirical model based on a climatological monthly means of the Linke turbidity (T_L) factor. Values of T_L for different regions of the world can be found on the Solar Radiation Data (SODA) website (http://www.soda-pro.com/).

Ceilometer measurements

Continuous vertical profiles of the backscattered laser signal were measured with a Vaisala CL31 Ceilometer based on the lidar technique, which uses light pulses sent to the atmosphere from a laser source. Subsequently, the Ceilometer measures the elastically-scattered waves returning to the surface [46]. The Vaisala CL31 uses an indium-gallium-arsenide pulsed-diode laser emitting 910 nm pulses at a repetition rate of 10 kHz. The device also uses a single lens for transmitting and receiving light. The maximum detectable cloud-base height of this instrument is 7500 m a.g.l. Backscattered profiles were recorded every 2 to 120 s at a maximum vertical resolution of 10 m [46].

HYSPLIT model

The 24-hour air-mass back-trajectories arriving at the AAO at the 500, 1000, and 1500 m a.g.l. were calculated using the Hybrid Single-Particle Lagrangian Integrated Trajectory Model (HYSPLIT) from the National Oceanic and Atmospheric Administration (NOAA). The HYSPLIT model allows computing simple air parcel trajectories of air pollutants [64]. The back trajectories for the 4 days of the HAP episode (i.e., May 14-17) were calculated using the Real-time Environmental Application and Display System (READY).

Declarations

Acknowledgments.

This study and Villanueva-Macias' fellowship were supported by the CONACYT grand "CB285023" and partially by DGAPA-UNAM, under grant IN-101719. The authors would like to thank OSR for providing the daily GHI data used in this study. The authors give special acknowledgment to physicist Roberto Hernandez for his technical assistance during the TEM analysis. The authors also express their gratitude for the SEM technical advice and sample treatment provide by Samuel Tehuacanero, Manuel Aguilar, and Diego Quiteiro from the LCM-IFUNAM.

Author contributions statement

G.C., and L.L., designed the research; G.C., J.M., M.S., H.A., and G.A performed the experiments and analyzed data; G.C. and J.M. performed a part of the TEM and EDS analysis; D.R. provided the GHI data and performed the ESRA model runs; M.G. operated the ceilometer and estimated the ML height. G.C. wrote the paper with contributions from J.M., L.L., and G.R.

Competing interests

The authors declare no competing interests.

References

1. Seinfeld, J. & Pandis, S. Atmospheric Chemistry and Physics: From Air Pollution to Climate Change 3rd edn. (Wiley, 2016).
2. Ching, J., Adachi, K., Zaizen, Y., Igarashi, Y. & Kajino, M. Aerosol mixing state revealed by transmission electron microscopy pertaining to cloud formation and human airway deposition. *npj Clim. Atmos. Sci.* **2**, 22 (2019). https://doi.org/10.1038/s41612-019-0081-9.
3. Lu, Q. *et al.* Atmospheric heating rate due to black carbon aerosols: Uncertainties and impact factors. *Atmos. Res.* **240**, 104891 (2020). https://doi.org/10.1016/j.atmosres.2020.104891.
4. Bellouin, N. *et al.* Bounding Global Aerosol Radiative Forcing of Climate Change. *Rev. of Geophys*. 58, e2019RG000660 (2020). https://doi.org/10.1029/2019RG000660.
5. Saidou Chaibou, A.A., Ma, X. & Sha, T. Dust radiative forcing and its impact on surface energy budget over West Africa. *Sci Rep.***10,** 12236 (2020). https://doi.org/10.1038/s41598-020-69223-4.

6. Ching, J., Kajino, M. Aerosol mixing state matters for particles deposition in human respiratory system. *Sci Rep.***8,** 8864 (2018). https://doi.org/10.1038/s41598-018-27156-z.
7. Zhang, L., Su, J., Huang, Y. *et al.*Examining the physical and chemical contributions to size spectrum evolution during the development of hazes. *Sci Rep.* **10,** 5347 (2020). https://doi.org/10.1038/s41598-020-62296-1.
8. Raga, G. B., Baumgardner, D., Castro, T., Martínez-Arroyo, A. & Navarro-González, R. Mexico City air quality: A qualitative review of gas and aerosol measurements (1960-2000). *Atmos. Environ.* **35**, 4041-4058 (2001). https://doi.org/10.1016/S1352-2310(01)00157-1.
9. Molina, L. T., Velasco, E., Retama, A. & Zavala, M. Experience from integrated air quality management in the Mexico City Metropolitan Area and Singapore. *Atmosphere*. **10**, 512 (2019). https://doi.org/10.3390/atmos10090512.
10. Ríos, B. & Raga, G. B. Spatio-temporal distribution of burnedareas by ecoregions in Mexico and Central America, International Journal of Remote Sensing, **39**, 949-970 (2018). http://doi.org/10.1080/01431161.2017.1392641
11. DeCarlo, P. F. *et al.* Fast airborne aerosol size and chemistry measurements above Mexico City and Central Mexico during the MILAGRO campaign. *Atmos. Chem. Phys.* **8**, 4027–4048 (2008). https://doi.org/10.5194/acp-8-4027-2008.
12. Yokelson, R. J. *et al.* Emissions from forest fires near Mexico City. *Atmos. Chem. Phys.* **7**, 5569–5584 (2007). https://doi.org/10.5194/acp-7-5569-2007.
13. Yokelson, R. J. *et al.* Emissions from biomass burning in the Yucatan. *Atmos. Chem. Phys.* **9**, 5785–5812 (2009). https://doi.org/10.5194/acp-9-5785-2009.
14. Salcedo, D. *et al.* Characterization of ambient aerosols in Mexico City during the MCMA-2003 campaign with Aerosol Mass Spectrometry: results from the CENICA Supersite. *Atmos. Chem. Phys.* **6**, 925–946 (2006). https://doi.org/10.5194/acp-6-925-2006.
15. Bäumer, D. *et al.* Relationship of visibility, aerosol optical thickness and aerosol size distribution in an ageing air mass over South-West Germany. *Atmos. Environ.* **42**, 989-998 (2008). https://doi.org/10.1016/j.atmosenv.2007.10.017.
16. Pósfai, M. *et al.* Atmospheric tar balls: Particles from biomass and biofuel burning. *J. Geophys. Res. D Atmos.* **109**, D06213 (2004). https://doi.org/10.1029/2003JD004169.
17. Pósfai, M. & Buseck, P. R. Nature and Climate Effects of Individual Tropospheric Aerosol Particles. *Annu. Rev. Earth Planet. Sci.* **38,** 17-43 (2010). https://doi.org/10.1146/annurev.earth.031208.100032.
18. Carabali, G. *et al.* Morphological and chemical characterization of soot emitted during flaming combustion stage of native-wood species used for cooking process in western Mexico. *J. Aerosol Sci.* **95**, 1-14 (2016). https://doi.org/10.1016/j.jaerosci.2016.01.008.
19. Carabali, G. *et al.* Optical properties, morphology and elemental composition of atmospheric particles at T1 supersite on MILAGRO campaign. *Atmos. Chem. Phys.* **12**, 2747–2755 (2012). https://doi.org/10.5194/acp-12-2747-2012.

20. Adachi, K. & Buseck, P. R. Internally mixed soot, sulfates, and organic matter in aerosol particles from Mexico City. *Atmos. Chem. Phys.* **8**, 6469–6481 (2008). https://doi.org/10.5194/acp-8-6469-2008.
21. Adachi, K. *et al.* Spherical tarball particles form through rapid chemical and physical changes of organic matter in biomass-burning smoke. *Proc. Natl. Acad. Sci. U. S. A.* **116**, 19336-19341 (2019). https://doi.org/10.1073/pnas.1900129116.
22. Buseck, P. R. & Pósfai, M. Airborne minerals and related aerosol particles: Effects on climate and the environment. *Proc. Natl. Acad. Sci. U. S. A.* **96**, 3372-3379 (1999). https://doi.org/10.1073/pnas.96.7.3372.
23. Brostrøm, A., Kling, K.I., Hougaard, K.S. *et al.*Complex Aerosol Characterization by Scanning Electron Microscopy Coupled with Energy Dispersive X-ray Spectroscopy. *Sci Rep* **10,** 9150 (2020). https://doi.org/10.1038/s41598-020-65383-5.
24. Jáuregui, E. The Climate of the Mexico City Air Basin: Its Effects on the Formation and Transport of Pollutants (eds. Fenn M. E., de Bauer, L. I., Hernández-Tejeda, T.) 86-117. (Springer-Verlag, 2002). https://doi.10.1007/978-0-387-22520-3_5.
25. Fast, J. D. & Zhong, S. Meteorological factors associated with inhomogeneous ozone concentrations within the Mexico City basin. *J. Geophys. Res. Atmos.* **103**, 18,927-18,946 (1998). https://doi.org/10.1029/98JD01725
26. Comisión Nacional Forestal (CONAFOR). Programa de Manejo del Fuego, Centro Nacional de Manejo del Fuego. *SEMARNAT* 1–17 https://www.gob.mx/cms/uploads/attachment/file/522446/Cierre_de_la_Temporada_2019.pdf (2019).
27. Hernández-López, A. E. *et al.* A study of PM2.5 elemental composition in southwest Mexico city and development of receptor models with positive matrix factorization. *Rev. Int. Contam. Ambient.* **37**, 67-88 (2021). http://dx.doi.org/10.20937/RICA.54066.
28. Tóth, A., Hoffer, A., Nyiro-Kósa, I., Pósfai, M. & Gelencsér, A. Atmospheric tar balls: Aged primary droplets from biomass burning? *Atmos. Chem. Phys.* **14**, 6669–6675 (2014). https://doi.org/10.5194/acp-14-6669-2014.
29. Gueymard, C. A. Temporal variability in direct and global irradiance at various time scales as affected by aerosols. *Sol. Energy* **86**, 3544-3553 (2012). https://doi.org/10.1016/j.solener.2012.01.013.
30. Rigollier, C., Bauer, O. & Wald, L. On the clear sky model of the ESRA - European Solar Radiation Atlas - With respect to the Heliosat method. *Sol. Energy* **68**, 33-48 (2000). https://doi.org/10.1016/S0038-092X(99)00055-9.
31. Schaaf, P., Stimac, J., Siebe, C. & Macías, J. L. Geochemical evidence for mantle origin and crustal processes in volcanic rocks from Popocatépetl and surrounding monogenetic volcanoes, central Mexico. *J. Petrol.* **46**, 1243-1282 (2005). https://doi.org/10.1093/petrology/egi015.
32. Grutter, M. *et al.* SO2 emissions from Popocatépetl volcano: Emission rates and plume imaging using optical remote sensing techniques. *Atmos. Chem. Phys.* **8**, 6655–6663 (2008).

https://doi.org/10.5194/acp-8-6655-2008.

33. Stremme, W., Ortega, I., Siebe, C. & Grutter, M. Gas composition of Popocatépetl Volcano between 2007 and 2008: FTIR spectroscopic measurements of an explosive event and during quiescent degassing. *Earth Planet. Sci. Lett.* **301**, 502-510 (2011). https://doi.org/10.1016/j.epsl.2010.11.032.
34. Chakrabarty, R. K. *et al.* Brown carbon in tar balls from smoldering biomass combustion. *Atmos. Chem. Phys.* **10**, 6363–6370 (2010). https://doi.org/10.5194/acp-10-6363-2010.
35. Hand, J. L. *et al.* Optical, physical, and chemical properties of tar balls observed during the Yosemite Aerosol Characterization Study. *J. Geophys. Res. Atmos.* **110**, D21210 (2005). https://doi.org/10.1029/2004JD005728.
36. Schill, G. P. *et al.* Widespread biomass burning smoke throughout the remote troposphere. *Nat. Geosci.* **13**, 422-427 (2020). https://doi.org/10.1038/s41561-020-0586-1.
37. Hernández Cerda, M. E., De Jesús Ordoñez Díaz, M. & Giménez de Azcárate, J. Comparative analysis of two bioclimatic classification systems applied in Mexico | Análisis comparativo de dos sistemas de clasificación bioclimática aplicados en México. *Investig. Geogr.* **95**, 2448-7279 (2018). https://doi.org/10.14350/rig.57451.
38. Vega, E. *et al.* Chemical composition of fine particles in Mexico City during 2003-2004. *Atmos. Pollut. Res.* **2**, 477-483 (2011). https://doi.org/10.5094/APR.2011.054.
39. Carabali, G. *et al.* Aerosol climatology over the Mexico City basin: Characterization of optical properties. *Atmos. Res.* **194**, 190–201 (2017). https://doi.org/10.1016/j.atmosres.2017.04.035.
40. Ying, Z., Tie, X., Madronich, S., Li, G. & Massie, S. Simulation of regional dust and its effect on photochemistry in the Mexico City area during MILAGRO experiment. *Atmos. Environ.* **45**, 2549-2558 (2011). https://doi.org/10.1016/j.atmosenv.2011.02.018.
41. Vega, E. *et al.* Chemical composition of fugitive dust emitters in Mexico City. *Atmos. Environ.* **35**, 4033-4039 (2001). https://doi.org/10.1016/S1352-2310(01)00164-9.
42. Baumgardner, D. *et al.* Physical and chemical properties of the regional mixed layer of Mexico's Megapolis. *Atmos. Chem. Phys.* **9**, 5711–5727 (2009). https://doi.org/10.5194/acp-9-5711-2009.
43. Roberts, G. C. *et al.* Characterization of particle cloud droplet activity and composition in the free troposphere and the boundary layer during INTEX-B. *Atmos. Chem. Phys.* **10**, 6627–6644 (2010). https://doi.org/10.5194/acp-10-6627-2010.
44. Zhou, S., Collier, S., Jaffe, D. A. & Zhang, Q. Free tropospheric aerosols at the Mt. Bachelor Observatory: More oxidized and higher sulfate content compared to boundary layer aerosols. *Atmos. Chem. Phys.* **19**, 1571–1585 (2019). https://doi.org/10.5194/acp-19-1571-2019.
45. Lee, T. E. *et al.* The NPOESS VIIRS day/night visible sensor. *Bull. Am. Meteorol. Soc.* **87**, 191-199 (2006). https://www.jstor.org/stable/26217142.
46. García-Franco, J.L., Stremme, W., Bezanilla, A. *et al.*Variability of the Mixed-Layer Height Over Mexico City. *Boundary-Layer Meteorol* **167,** 493–507 (2018). https://doi.org/10.1007/s10546-018-0334-x.

47. Whiteman, C. D., Zhong, S., Bian, X., Fast, J. D. & Doran, J. C. Boundary layer evolution and regional-scale diurnal circulations over the Mexico Basin and Mexican plateau. *J. Geophys. Res. Atmos.* **105**, 10081–10102 (2000). https://doi.org/10.1029/2000JD900039.

48. Pereira, D. L. *et al.* Characterization of ice nucleating particles in rainwater, cloud water, and aerosol samples at two different tropical latitudes. *Atmos. Res.* **250**, 105356 (2021). https://doi.org/10.1016/j.atmosres.2020.105356.

49. Peralta, O., Adams, D., Castro, T., Grutter, M. & Varela, A. Mexico's University Network of Atmospheric Observatories. *Eos,* **97** (2016). https://doi:10.1029/2016EO045273.

50. Baylon, J. L., Stremme, W., Grutter, M., Hase, F. & Blumenstock, T. Background CO2 levels and error analysis from ground-based solar absorption IR measurements in central Mexico. *Atmos. Meas. Tech.* **10**, 2425–2434 (2017). https://doi.org/10.5194/amt-10-2425-2017.

51. Campion, R. *et al.* Breathing and coughing: The extraordinarily high degassing of popocatépetl volcano investigated with an So2 camera. *Front. Earth Sci.* **6**. (2018). https://doi.org/10.3389/feart.2018.00163.

52. Carabalí, G. *et al.* Aerosol Optical Characteristics During the Biomass Burning Season in Southeastern Mexico. *Water. Air. Soil Pollut.* **230**, 241 (2019). https://doi.org/10.1007/s11270-019-4284-9

53. Rios, B. & Raga, G. B. Smoke emissions from agricultural fires in Mexico and Central America. *J. Appl. Remote Sens.* **13**, 036509 (2019). https://doi:10.1117/1.JRS.13.036509.

54. Taquet, N. *et al.* Continuous measurements of SiF4 and SO2 by thermal emission spectroscopy: Insight from a 6-month survey at the Popocatépetl volcano. *J. Volcanol. Geotherm. Res.* **341**, 255–268 (2017). https://doi.org/10.1016/j.jvolgeores.2017.05.009

55. Taquet, N. *et al.* Variability in the gas composition of the popocatépetl volcanic plume. *Front. Earth Sci.* **7**, (2019). https://doi.org/10.3389/feart.2019.00114

56. Marple, V. A., Rubow, K. L. & Behm, S. M. A microorifice uniform deposit impactor (moudi): Description, calibration, and use. *Aerosol Sci. Technol.* **14**, 434–436 (1991). https://doi.org/10.1080/02786829108959504

57. Córdoba, F. *et al.* Measurement report: Ice nucleating abilities of biomass burning, African dust, and sea spray aerosol particles over the Yucatan Peninsula. *Atmos. Chem. Phys.* **21,** 4453–4470, (2021). https://doi.org/10.5194/acp-21-4453-2021

58. Espinosa, A. A. *et al.* Development of an X-ray fluorescence spectrometer for environmental science applications. *Instrum. Sci. Technol.* **40**, 603-617 (2012). https://doi.org/10.1080/10739149.2012.693560

59. Nakayama, T. *et al.* Characterization of a three wavelength photoacoustic soot spectrometer (Pass-3) and a photoacoustic extinctiometer (pax). *J. Meteorol. Soc. Japan* **93**, 285-308 (2015). https://doi.org/10.2151/jmsj.2015-016

60. Holben, B. N. *et al.* AERONET - A federated instrument network and data archive for aerosol characterization. *Remote Sens. Environ.* **66**, 1–16 (1998). https://doi.org/10.1016/S0034-

4257(98)00031-5

61. O'Neill, N. T. *et al.* Bimodal size distribution influences on the variation of Angstrom derivatives in spectral and optical depth space. *J. Geophys. Res. Atmos.* **106**, 9787–9806 (2001). https://doi.org/10.1029/2000JD900245
62. Giles, D. M. *et al.* Advancements in the Aerosol Robotic Network (AERONET) Version 3 database - Automated near-real-time quality control algorithm with improved cloud screening for Sun photometer aerosol optical depth (AOD) measurements. *Atmos. Meas. Tech.* **12**, 169–209 (2019). https://doi.org/10.5194/amt-12-169-2019
63. Smirnov, A., Holben, B. N., Eck, T. F., Dubovik, O. & Slutsker, I. Cloud-screening and quality control algorithms for the AERONET database. *Remote Sens. Environ.* **73**, 337–349 (2000). https://doi.org/10.1016/S0034-4257(00)00109-7
64. Stein, A. F. *et al.* Noaa's hysplit atmospheric transport and dispersion modeling system. *Bull. Am. Meteorol. Soc*. **96**, 2059-2077 (2015). https://doi.org/10.1175/BAMS-D-14-00110.1

Figures

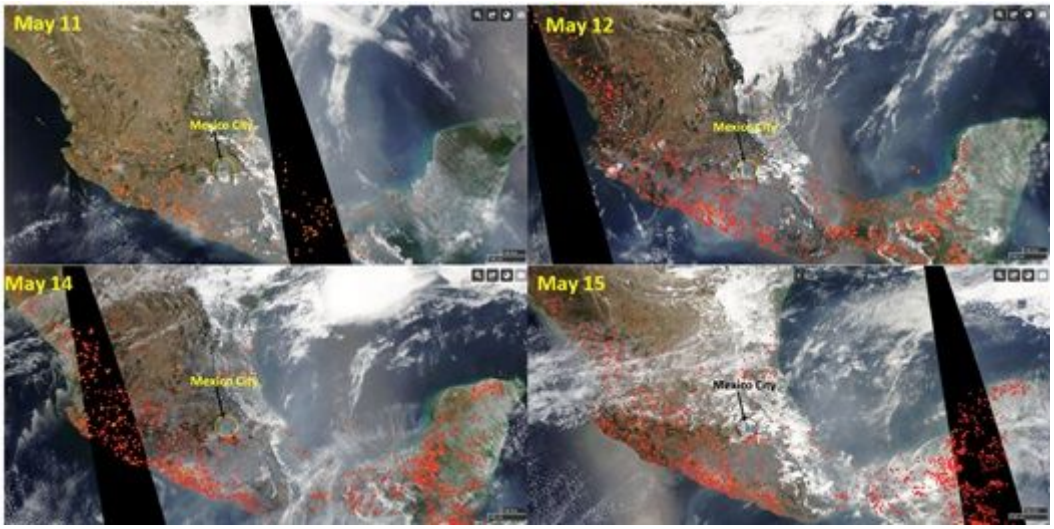

Figure 1

Spatial distribution of active fires (red dots) in Mexico detected by the Visible Infrared Imaging Radiometer Suite (VIIRS) between May 11 and 15, 2019. (Courtesy NASA, https://worldview.earthdata.nasa.gov).

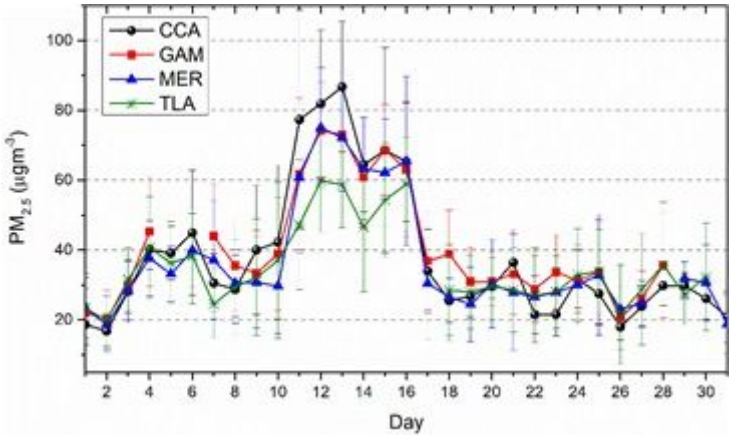

Figure 2

Time series of the 24-hourly means of the PM2.5 concentration during May 2019. Data were plotted for the four RAMA stations: CCA (black), GAM (red), MER (blue), and TLA (green).

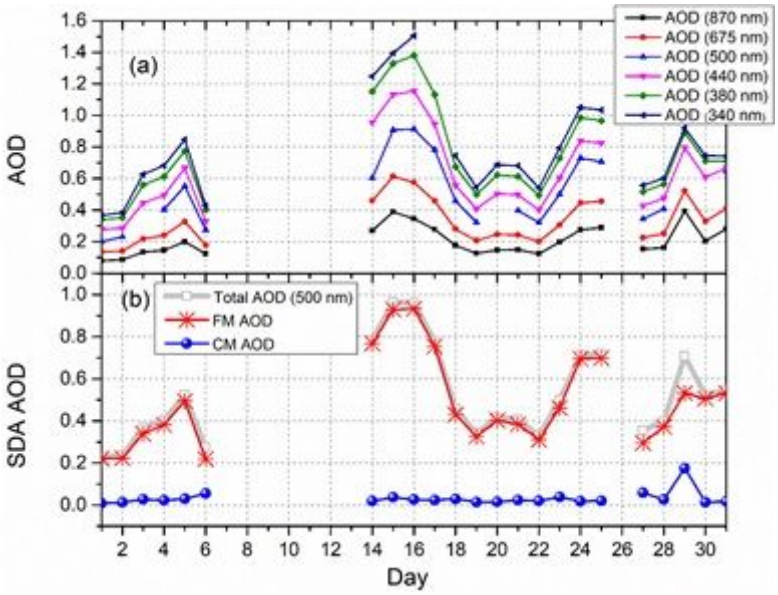

Figure 3

a) Time series of AOD at 6 wavelengths (340, 380, 440, 500, 675, and 870) and b) SDA retrievals of the FM and CM contributions to the total AOD at 500 nm.

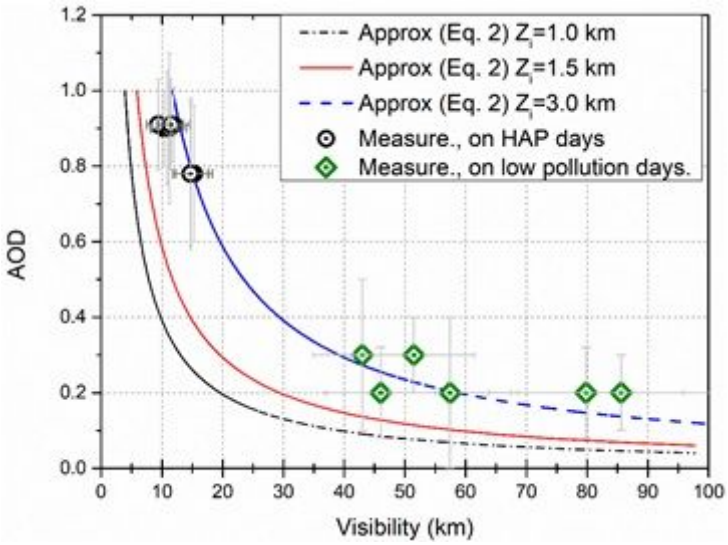

Figure 4

Visibility as a function of AOD values (at what wavelength?) from AERONET. Visibility is estimated from βext (532 nm) and calculated using Eq. 2.

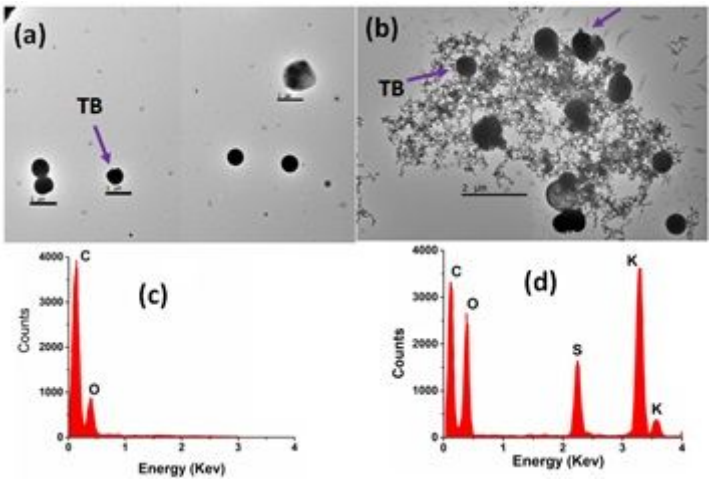

Figure 5

TEM images of the a) TB and b) Soot particles, and EDS spectra of: c) TB and d) soot particles sampled in MC.

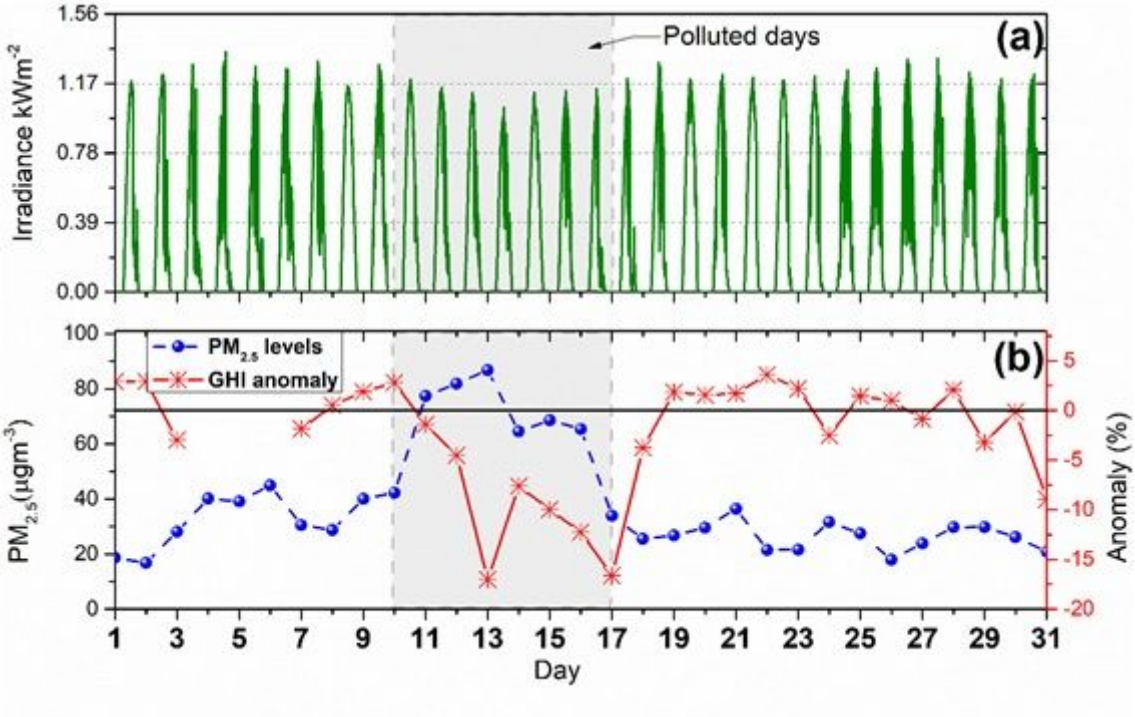

Figure 6

(a) Daily GHI measurements and (b) Hourly GHI percent anomaly (solid red line) compared with the daily mean PM2.5 concentration (blue dashed line) measured at CCA stations in MC during May 2019.

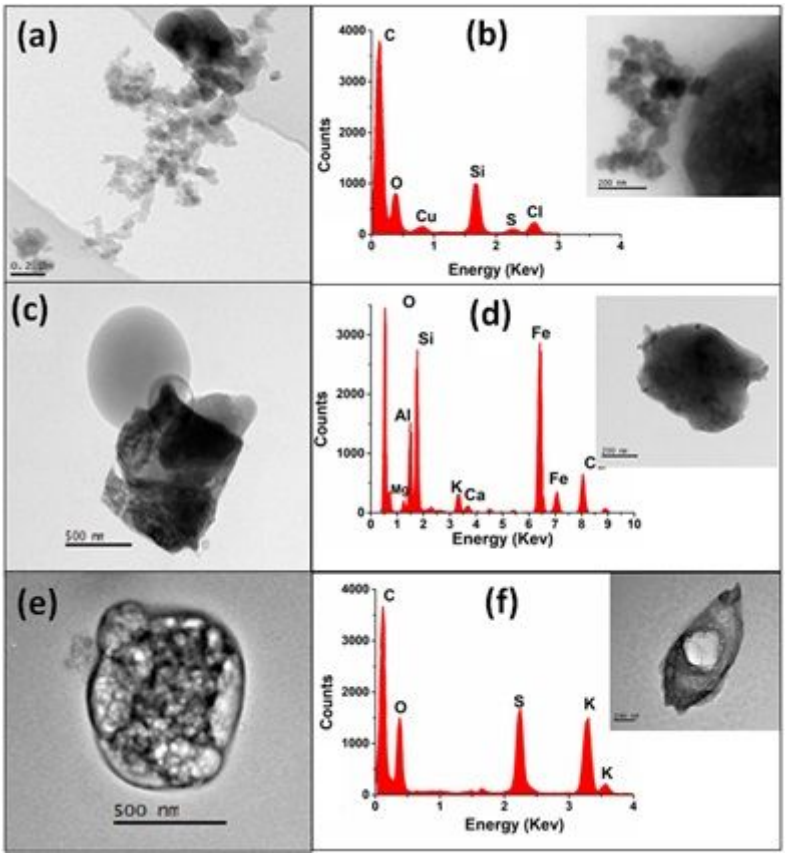

Figure 7

High-magnification TEM micrographs and EDS spectra for: a) and B) soot aggregates; c) and d) mineral dust; d) and e) S-rich particles.

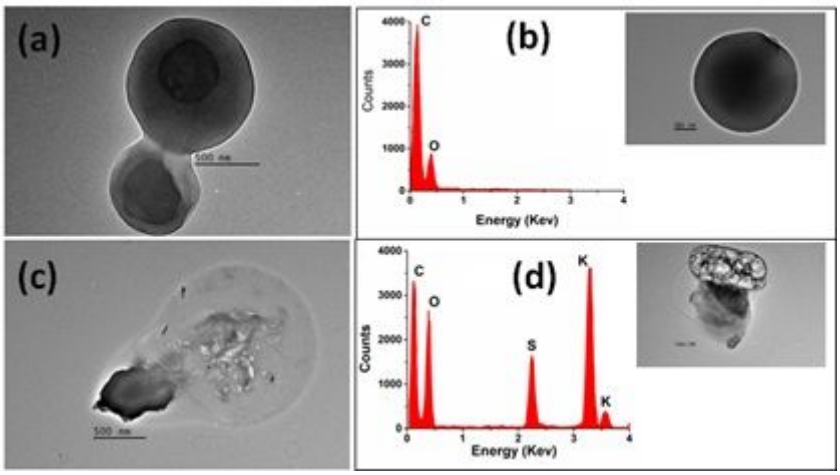

Figure 8

High-magnification TEM micrographs and EDS spectra for: a) and B) Tarballs; c) and d) Secondary aerosols particles.

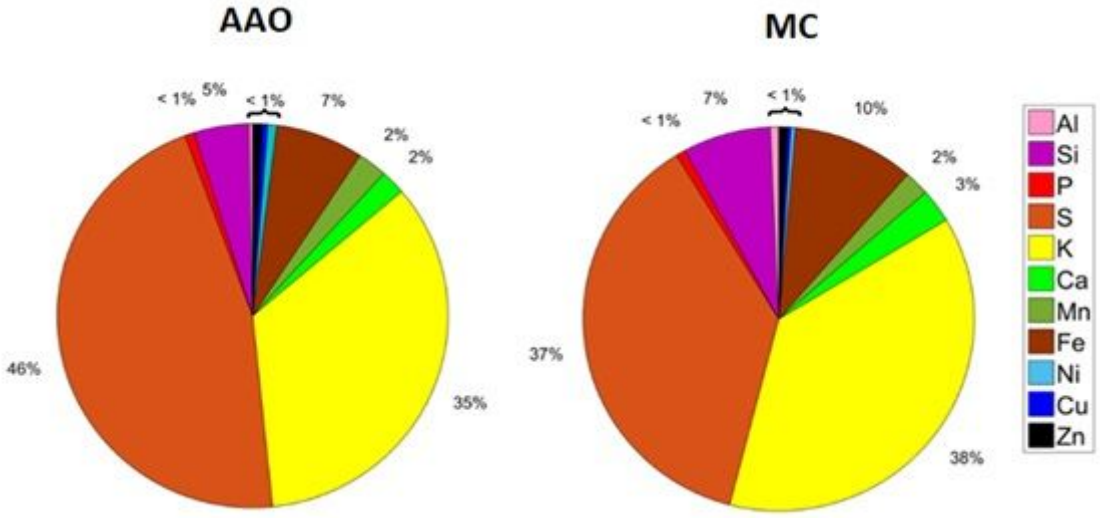

Figure 9

Pie charts of the elemental composition (determined by XRF) of atmospheric particles sampled in two different sites a) AAO and b) MC during the HAP event.

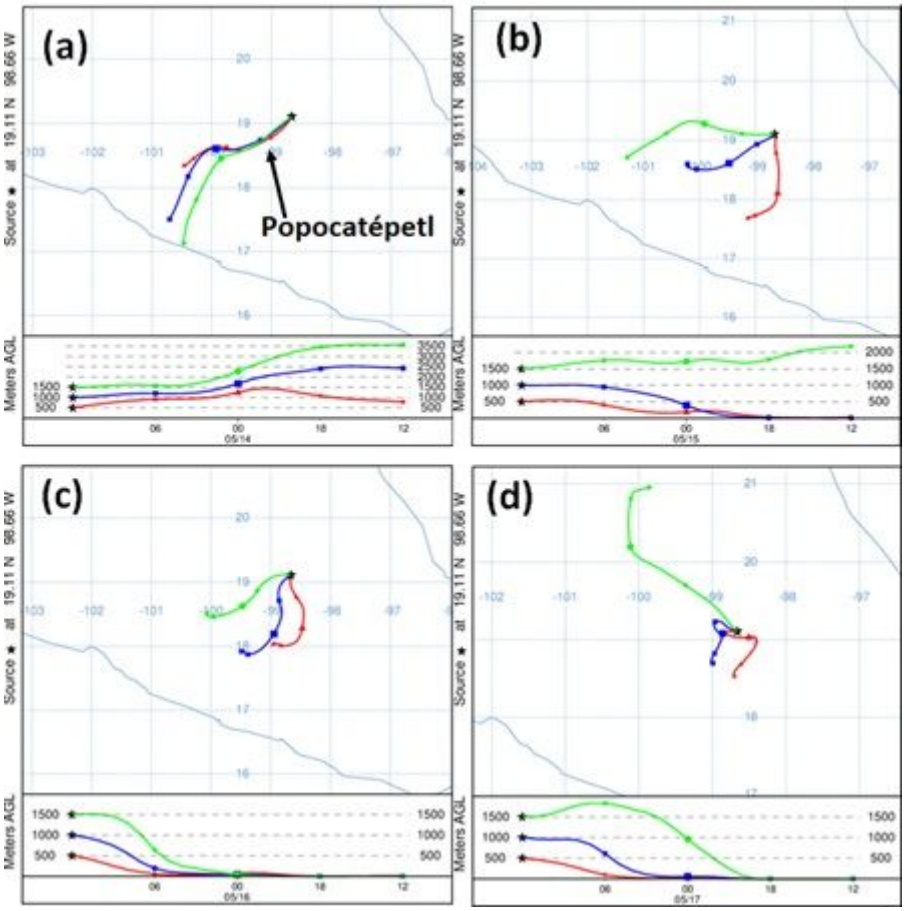

Figure 10

The 24-h backward simulation using the NOAA HYSPLIT model for air masses arriving at the AAO at different heights (100, 500, and 1000 above ground level) for sampling days a) 13, b) 14, c) 16 and d) May 17 2019.

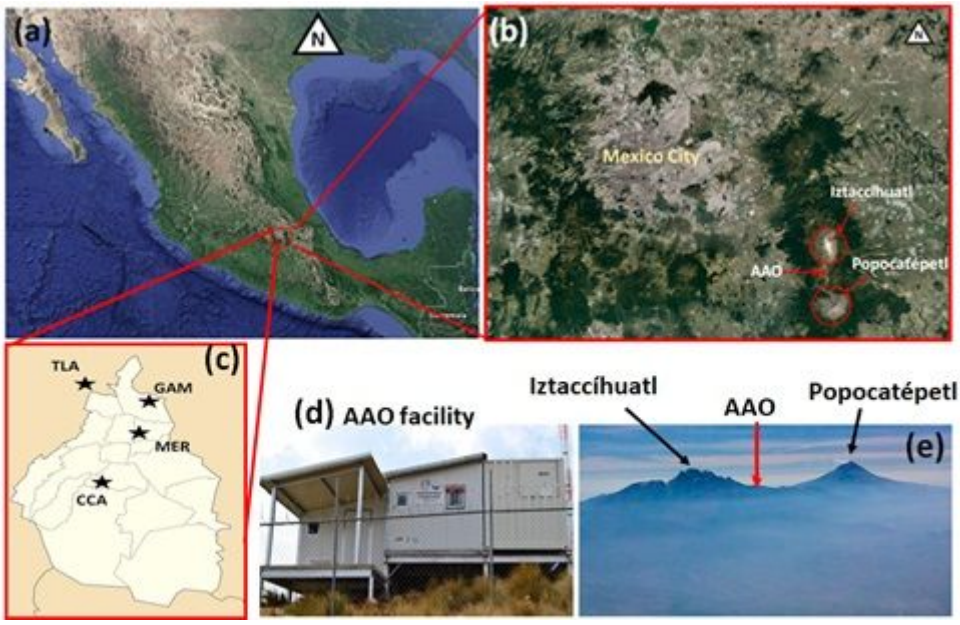

Figure 11

Geographical area under study. a) Map of Mexico with an inset indicating the sampling site, b) Satellite image showing the location of MC, the AAO, and the nearby volcanoes, c) Location of the four RAMA stations in MC, (d) The AAO facility, and e) A panoramic view of the Popocatepetl and the Iztaccihualt volcanoes.

Supplementary Files

This is a list of supplementary files associated with this preprint. Click to download.

- SupportinginformationSR.docx